Wavelength Dependence of Ultrahigh-Resolution Optical Coherence Tomography Using Supercontinuum for Biomedical Imaging

Norihiko Nishizawa, *Member, IEEE*, Hiroyuki Kawagoe, Masahito Yamanaka, Miyoko Matsushima, Kensaku Mori, and Tsutomu Kawabe

(Invited Paper)

***Abstract*—Optical coherence tomography (OCT) is a noninvasive cross-sectional imaging technique with micrometer resolution. The theoretical axial resolution is determined by the center wavelength and bandwidth of the light source, and the wider the bandwidth, the higher the axial resolution. The characteristics of OCT imaging depend on the optical wavelength used. In this paper, we investigated the wavelength dependence of ultrahigh-resolution (UHR) OCT using a supercontinuum for biomedical imaging. Wideband, high-power, low-noise supercontinua (SC) were generated at $\lambda = 0.8$, 1.1, 1.3, and 1.7 μm based on ultrashort pulses and nonlinear fibers. The wavelength dependence of OCT imaging was examined quantitatively using biological phantoms. Ultrahigh-resolution imaging of a rat lung was demonstrated with $\lambda = 0.8$–1.0 μm UHR-OCT. The variation of alveolar volume was estimated using three-dimensional image analysis. Finally, UHR-spectral domain-OCT and optical coherence microscopy at 1.7 μm were developed, and high-resolution and high-penetration imaging of turbid tissue, especially mouse brain, was demonstrated.**

***Index Terms*—Optical coherence tomography, supercontinuum, optical coherence microscopy, fiber lasers, ultrashort pulse.**

I. Introduction

OPTICAL coherence tomography, abbreviated OCT, is a non-invasive, micrometer-scale cross-sectional imaging technique using an optical interferometer [1]. Since OCT is a non-invasive technique for imaging internal structure, it has been applied in the medical field, especially in ophthalmology [2], [3]. It has been already used at the clinical stage, especially for observing cross-sections of the retina.

Manuscript received April 11, 2018; revised June 29, 2018; accepted June 30, 2018. Date of publication July 9, 2018; date of current version July 26, 2018. *(Corresponding author: Norihiko Nishizawa.)*

N. Nishizawa, H. Kawagoe, and M. Yamanaka are with the Department of Electrical Engineering and Computer Science, Nagoya University, Nagoya, Aichi 464-8603, Japan (e-mail: nishizawa@nuee.nagoya-u.ac.jp; kawagoe@ap.eng.osaka-u.ac.jp; yamanaka@nuee.nagoya-u.ac.jp).

M. Matsushima and T. Kawabe are with the Graduate School of Medicine, Nagoya University, Nagoya, Aichi 466-8550, Japan (e-mail: matsu@met.nagoya-u.ac.jp; kawabe@met.nagoya-u.ac.jp).

K. Mori is with the Graduate School of Informatics, Nagoya University, Nagoya, Aichi 464-8601, Japan (e-mail: kensaku@is.nagoya-u.ac.jp).

Color versions of one or more of the figures in this paper are available online at http://ieeexplore.ieee.org.

Digital Object Identifier 10.1109/JSTQE.2018.2854595

Three main schemes are used for OCT imaging: time-domain (TD) OCT, spectral-domain (SD) OCT, and swept-source (SS) OCT. The theoretical axial resolution is determined by the coherence length of the light source, and the wider the spectral bandwidth is, the higher the axial resolution is. For SS-OCT, a rapid-wavelength-tunable cw laser is used as the light source, and the interference signal is observed in the spectral domain. The axial resolution is, in this case, limited by the bandwidth of the light source. For TD-OCT and SD-OCT, ultrahigh-resolution OCT has been demonstrated using a wideband supercontinuum (SC) [4], [5]. An SC is an ultrawideband spectrum broadened by nonlinear effects. It used to be necessary to use a high-energy short pulse to achieve a wideband SC [6], [7]. Thanks to the invention of highly nonlinear fibers and photonic crystal fibers, since they can confine the optical power inside a small core area along a long length, a wideband SC can now be achieved with nJ pulses. Nowadays, SC sources are commercially available, and they have been applied to ultrahigh-resolution OCT [8]–[10].

We have been investigating ultrahigh-resolution OCT using SC sources [11]. The characteristics of OCT imaging depend on the optical wavelength used. We have constructed SC and OCT systems operating in different wavelength ranges, and we have been investigating the wavelength dependence of OCT imaging [12]–[16].

In this paper, we investigated the wavelength dependence of UHR-OCT using an SC, for application to biomedical imaging. First, we discuss SC generation for UHR-OCT. Then, we describe experiments in which we prepared lipid samples, and investigated the wavelength dependence of OCT imaging both qualitatively and quantitatively. Then, considering the wavelength dependence results, we demonstrated biomedical imaging using animal samples. First, we investigated OCT imaging of rat lung tissue via a collaboration between medical and software groups. 3D imaging analysis was demonstrated for investigating alveolar structures. Then, we developed UHR-OCT systems operating in the $\lambda = 1.7$ μm range using a high-power SC for deep imaging of turbid tissues. High-resolution SD-OCT and optical coherence microscopy (OCM) systems were developed, and the characteristics were examined through imaging of mouse brain samples.

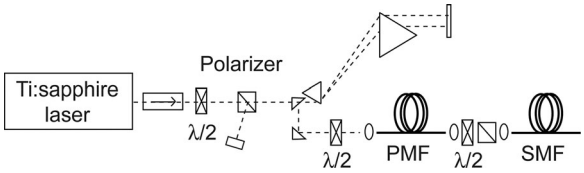

Fig. 1. Experimental setup of coherent SC generation with ultrashort pulse solid state laser and optical fiber.

II. Supercontinuum Generation for Ultrahigh-Resolution OCT

The operating principle of OCT is like that of an incoherent interferometer. The theoretical axial resolution, Δz, is equal to the coherence length and is written as

$$\Delta z = 2\ln 2/\pi \cdot \lambda^2/\Delta\lambda \tag{1}$$

where λ is the center wavelength, and $\Delta\lambda$ is the bandwidth of the light source [2], [3]. Therefore, the wider the bandwidth of the light source is, the higher the axial resolution is.

Another important requirement for the light source in OCT is low noise. For the OCT imaging of biological samples, a high sensitivity of up to 90 dB is required. The higher the sensitivity is, the deeper the penetration is. The noise properties of the light source directly affect the sensitivity of OCT imaging, so a low-noise, wideband light source is ideal for UHR-OCT imaging.

We have been investigating UHR-OCT imaging using wideband light sources. As an example of such a wideband light source, we have been investigating the supercontinuum generated with an ultrashort pulse and optical fibers.

There are many reports of ultrawideband SC generation using photonic crystal fibers and highly nonlinear fibers [6], [7]. Ultrawideband SC generation can be demonstrated using an SC generation scheme based on highly nonlinear fibers including photonic crystal fibers pumped around the zero-dispersion wavelength. The wideband SC can be generated by pumping with cw laser light or laser pulses whose pulse widths are wider than picoseconds. However, in this case, the pump beam is divided into multiple ultrashort pulses, and they generate lots of different SCs. As a result, although the optical spectra of the generated SCs look smooth when averaged, each SC has a different spectral shape for one shot and contains high-intensity noise [17], [18].

Using an ultrashort pulse and normally dispersive highly nonlinear fibers, the spectrum was broadened by only self-phase modulation, and there was no temporal overlap among the spectral components of the SC. As a result, we could generate a low-noise, highly coherent, and smooth SC [19]–[21]. The spectral shape is another important factor. For the SC generated with normally dispersive fibers and an ultrashort pulse, the spectral shape is smooth and consists of a single peak, making it suitable for UHR-OCT.

Figure 1 shows the configuration for SC generation using an ultrashort pulse laser and optical fibers. This scheme has been used for SC generation at $\lambda = 0.8$ and 1.0 μm [12], [13]. The ultrashort pulse generated by a passively mode-locked solid state laser was used as the pump pulse. The spectral and temporal

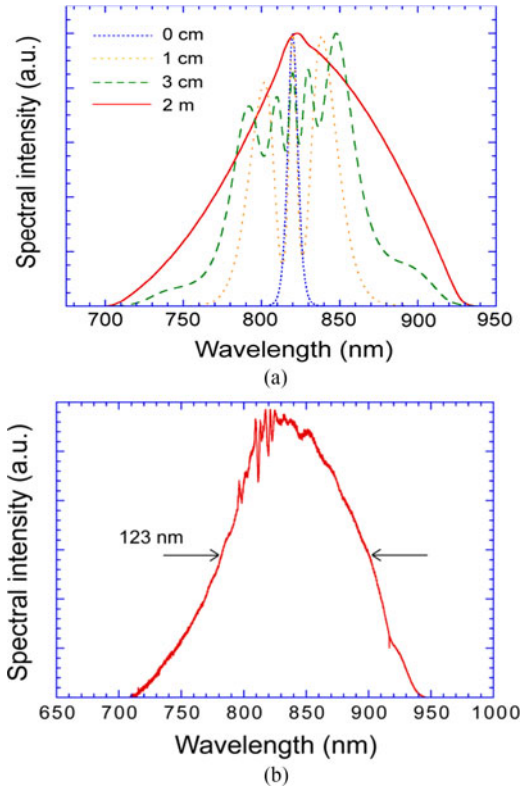

Fig. 2. Supercontinuum generation in normal dispersive optical fibers, (a) numerical results of SC generation and (b) experimentally generated spectrum.

shapes of the output pulse were sech^2, and the temporal width was $\sim$100 fs. In the 0.8 μm range, since the output pulse had a slight chirp owing to the chromatic dispersion of the optical isolator and the optical devices in the laser, dispersion compensation with a prism pair was applied, as shown in Fig. 1. Then the ultrashort pump pulse was coupled into the optical fibers, and the SC was generated.

Figure 2(a) shows the numerical results of the SC generation scheme shown in Fig. 1. The optical spectrum rapidly broadened through self-phase modulation within a few cm of the optical fiber. The spectral shape had a few peaks, which are typical characteristics of self-phase modulation. Then, the spectral shape became gradually smoother along with the propagation in the normally dispersive fibers. After 2 m of propagation, a smooth Gaussian-like wideband SC was generated.

Figure 2(b) shows the optical spectrum of the generated SC in the experiment. It had a Gaussian-like smooth shape, which is almost in agreement with the numerical one. The noise properties and coherence were examined, and it was confirmed that the SC had low noise and high coherence properties. The corresponding theoretical axial resolution was 2.0 μm.

For the SC generation at 0.8 μm, an ultrashort-pulse Ti:Sapphire laser (MaiTai) and polarization maintaining fiber with a small core were used [12]. Recently, generation of a Gaussian-like SC was demonstrated using photonic crystal fiber (PCF) and the SHG pulse from an Er-doped ultrashort-pulse fiber laser system [22].

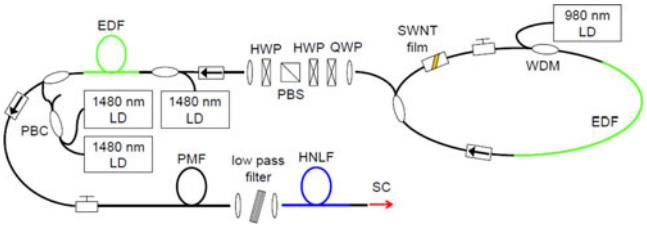

Fig. 3. Experimental setup of SC generation at $\lambda = 1.7\ \mu$m based on Er-doped ultrashort pulse fiber laser with SWNT.

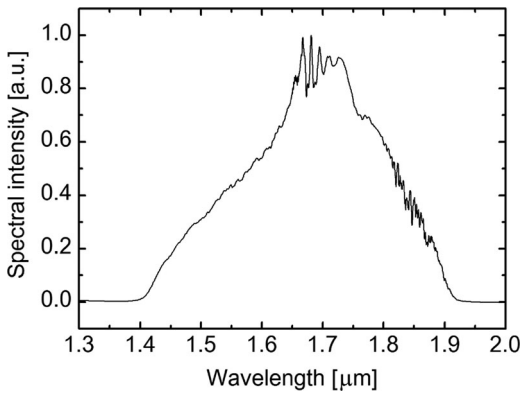

Fig. 4. Optical spectrum of generated SC at $\lambda = 1.7\ \mu$m.

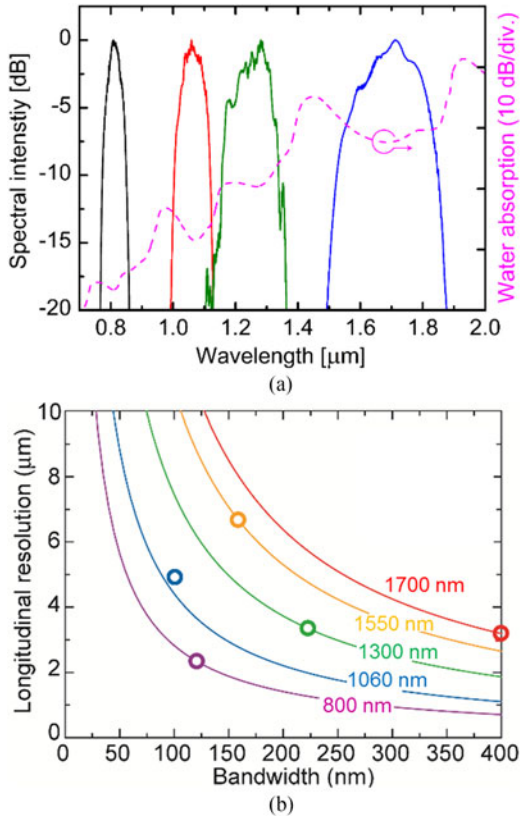

Fig. 5. (a) Spectra of generated SC for OCT. (b) Relation between axial resolution and bandwidth of light source for examined wavelengths. The symbols correspond to the generated SCs in this work.

For SC generation at 1.0 μm, a SESAM mode-locked ultrashort-pulse Nd:glass laser was used as the pump pulse source. It generated a 100 fs transform-limited sech^2 pulse at 1.06 μm. The output pulse was coupled into UHNA3 fiber having normal dispersion properties and a small core. This scheme also generated a Gaussian-like SC [23].

For generating an SC at 1.3 μm, we started with an Er-doped ultrashort-pulse fiber laser system. The output pulse was amplified in an Er-doped fiber amplifier, and a wideband SC centered at 1.55 μm was generated. The 1.3 μm component was picked off with a bandpass filter to obtain the SC at 1.3 μm [13].

Figure 3 shows a configuration for SC generation at 1.7 μm [16], using a passively mode-locked ultrashort-pulse fiber laser and a single wall carbon nanotube (SWNT) film. This setup generated $\sim$250 fs sech^2-shaped ultrashort pulses at a repetition frequency of 110 MHz. The output pulses were introduced into an Er-doped fiber amplifier to generate high-power ultrashort pulses, which were introduced into PMF, generating Raman-shifted soliton pulses at 1.7 μm. The output pulses were passed through a low pass filter, and only the soliton pulse was coupled into normally dispersive highly nonlinear fiber, generating a Gaussian-like SC, as shown in Fig. 4. The average power was 60 mW. The corresponding theoretical axial resolution was 3.1 μm.

Figure 5(a) shows the optical spectra of a generated SC, and the absorption spectra of water. In biological tissue, there are strong absorptions by hemoglobin and water. In highly transparent tissue, like the eye, the absorption by water is dominant, and the wavelength range of 0.8–1.0 μm has been mainly used for observation of the fundus of the eye. In conventional tissue, the absorption by hemoglobin, which is larger at shorter wavelengths, is dominant, and the wavelength range of 1.3 μm has been mainly used. In terms of scattering, the longer the wavelength is, the lower the magnitude of the scattering is. Recently, much attention has been focused on longer wavelengths for deep tissue imaging.

Figure 5(b) shows the relation between axial resolution and bandwidth of the light source [13]. The symbols correspond to the generated SC in this work. From eq. (1), the shorter the wavelength is, the higher the axial resolution is for the same bandwidth. In other words, a wideband spectrum is required for demonstrating ultrahigh-resolution OCT at longer wavelengths.

III. Wavelength Dependence of UHR-OCT

In biological samples, since the magnitudes of absorption and scattering depend on the wavelength, the characteristics of OCT imaging depend on the optical wavelength. In our previous work, we investigated the wavelength dependence of OCT imaging using several different samples. In this work, in order to discuss the wavelength dependence of OCT imaging, we prepared a biological tissue phantom, and we performed a quantitative comparison of OCT imaging in four wavelength regions, including the 1.7 μm band. As the wavelengths, we used 0.8 μm, which is commonly used for ophthalmic imaging, and 1.1 μm and 1.3 μm, which have been used for deep tissue imaging recently.

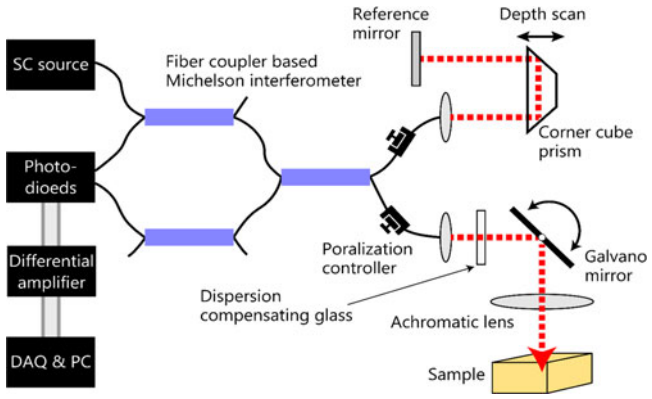

Fig. 6. Experimental setup of time-domain OCT for the investigation of wavelength dependence.

TABLE I
EXPERIMENTAL CONDITIONS AT EACH WAVELENGTH

Wavelength [μm]	Sensitivity [dB]	Axial res. [μm]	Rayleigh range [mm]	Return power from sample mirror [μW]
0.8	90.4	5.1	0.27	~100
1.1	92.0	5.2	0.28	~100
1.3	90.6	5.4	0.29	~100
1.7	88.4	5.2	0.37	~100

Figure 6 shows the experimental setup of the TD-OCT system for investigating the wavelength dependence. In order to discuss the wavelength dependence of OCT imaging, we have to adjust the characteristics of OCT imaging at each wavelength. In this work, the sensitivity, optical power falling on the detector, and Rayleigh length in front of the sample were adjusted at each wavelength. The characteristics of the OCT systems used in this work are shown in Table I.

As the OCT light source, we used an SC generated with ultrashort laser pulses and highly nonlinear fibers. The schemes of SC sources used in this work were mentioned in the previous section. In order to maintain the same conditions, we controlled the magnitude of the nonlinearity, and the bandwidth of SC was adjusted to achieve a longitudinal axial resolution of 5 μm in tissue.

A. Biological Tissue Phantom Using Lipid Mixture

In this work, we investigated the OCT imaging characteristics quantitatively using a biological tissue phantom, in which the optical properties can be arbitrary controlled. The main target of imaging in this study is a highly scattering sample containing water, such as brain and skin. In place of the highly scattering tissue, we used lipid mixtures as the biological tissue phantom, which have a high scattering coefficient and high water content. Since we can control the scattering and absorption coefficients arbitrarily by controlling the ratio of lipid droplets and H_2O, a

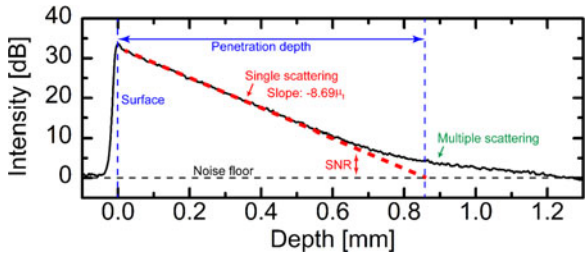

Fig. 7. Example of OCT signal intensity profile observed in biological tissue phantom.

biological tissue phantom consisting of a lipid mixture is often used for the quantitative characterization of biomedical imaging [24], [25]. In order to examine the variation in penetration depth and image contrast in OCT imaging as a function of the scattering coefficient of the biological tissue, a 20% lipid solution was diluted with water (H_2O) and heavy water (D_2O) to prepare lipid mixtures with lipid densities of 1, 2, 3, 5, 8, 10, and 15%. The optical absorption properties of brain and skin in the near infrared region coincide with that of 70% water. In order to realize the absorption properties of highly scattering tissue, we added heavy water (D_2O) into the mixture so that the absorption property coincided with that of the 70% volume density water [26]–[28]. In this work, the refractive index of the phantom was assumed to be constant at 1.35 at wavelengths of 0.8–1.7 μm, and we investigated the wavelength dependence.

B. Definition of Penetration Depth and Contrast (SNR) in OCT Imaging

For the OCT measurement of a sample that has a homogeneous structure and a constant index distribution along the longitudinal direction, the behavior of the decreasing OCT signal is explained with the "single scattering model" [28]–[30]. The single scattering model is used for investigating the optical attenuation inside the sample under assumption that the scattering occurs only once inside the sample. The biological phantom (lipid mixture) used in this work had a homogeneous structure and a constant index distribution along the longitudinal direction on a macro scale, and therefore, the single scattering model was used to determine the imaging depth and contrast in OCT imaging. In the single scattering model, the OCT signal power $P(z)$ coming back from a point at depth z from the surface decreases exponentially as

$$P(z) = P_0 \exp(-\mu_t \cdot 2z), \tag{2}$$

where P_0 represents the OCT signal power from the sample surface, and μ_t is the attenuation constant. Taking the log of eq. (2), we obtain

$$10 \cdot \log_{10}\left(\frac{P(z)}{P_0}\right) = -20\mu_t \cdot \log_{10} e \cdot z \approx -8.69\mu_t \cdot z. \tag{3}$$

Therefore, the log of the OCT signal power decreases linearly as a function of the depth.

Figure 7 shows the depth profile of the OCT signal power in the biological phantom measurement. The solid lines represent

the observed OCT signal power, and the broken lines show the attenuation line obtained by the single scattering model. In order to reduce the variation in signal power, the depth profile of the OCT signal was averaged 900 times at the same line. Around the sample surface, the OCT signal power decreased linearly along the measurement depth, and we can see that the single scattering model was usable. At the deep part of the sample, the measurement value was larger than the line estimated by the single scattering model. It is considered that these signals are affected by artifacts caused by multiple scattering, and the actual noise floor at the deep part was increased by the effect of multiple scattering events [29]. In this work, we define the imaging depth as the length from the sample surface to the depth where the straight line obtained by the single scattering model crosses the noise floor, as shown in Fig. 7. We also define the imaging contrast (SNR) as the ratio between the values of a straight line obtained by the single scattering model and that of the noise floor at each depth. We examined these parameters at different wavelengths, and discuss the wavelength dependence of OCT imaging.

C. *Wavelength Dependence of OCT Imaging*

Here, we used biological phantoms with different lipid densities, and we examined the dependence of the imaging depth and image contrast in OCT imaging on the effect of scattering coefficients and optical wavelength.

The results of OCT imaging in biological phantoms are shown in Fig. 8. For a phantom with 1% lipid density, the imaging depth at $\lambda = 1.7$ μm was obviously shorter than those at $\lambda = 1.1$ and 1.3 μm, owing to the effect of water absorption. As for the imaging contrast, the SNR was $\sim$20 dB at $\lambda = 0.8$–1.3 μm, whereas it was $\sim$10 dB at $\lambda = 1.7$ μm at a depth of $\sim$0.5 mm. It is considered that the scattering magnitude was the smallest and the power of scattered light decreased at $\lambda = 1.7$ μm among the four wavelengths examined.

At $\lambda = 0.8$–1.3 μm, as the lipid density increased and the magnitude of scattering inside the phantom increased, the image contrast around the sample surface increased, but the imaging depth obviously decreased owing to signal attenuation by scattering. For the phantoms having 8% and 15% lipid densities, the deepest penetration depth was obtained at $\lambda = 1.7$ μm, where the effect of scattering was minimum among the four wavelengths. For $\lambda = 1.7$ μm, as the lipid density in the sample increased, the OCT image contrast increased at the deep part, as well as around the surface.

From the depth profile of the OCT signal power in the phantom, as shown in Fig. 7, we obtained the attenuation coefficient using the single scattering model. Fig. 9(a) shows the attenuation coefficient obtained with the single scattering model. At $\lambda = 1.7$ μm, the attenuation coefficient was almost constant while the magnitude of the scattering coefficient increased. On the other hand, the OCT signal intensity increased as the lipid density increased. As a result, the image contrast at a deep part increased at $\lambda = 1.7$ μm as the lipid density increased.

For $\lambda = 0.8$–1.3 μm, the attenuation coefficient obviously increased as the lipid density increased [Fig. 9(a)]. In addition,

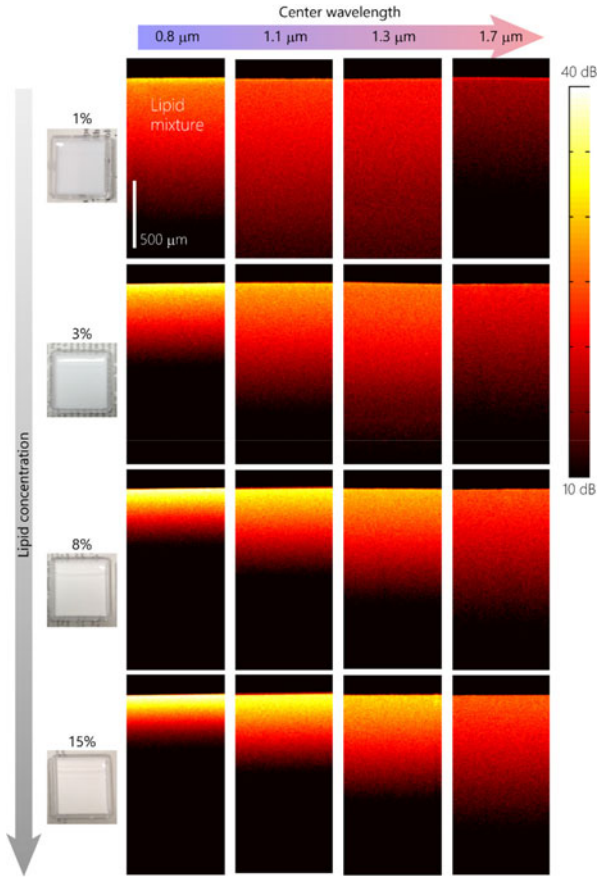

Fig. 8. Observed OCT images of biological phantom as the functions of wavelength and lipid concentration. The horizontal scan range was 1 mm.

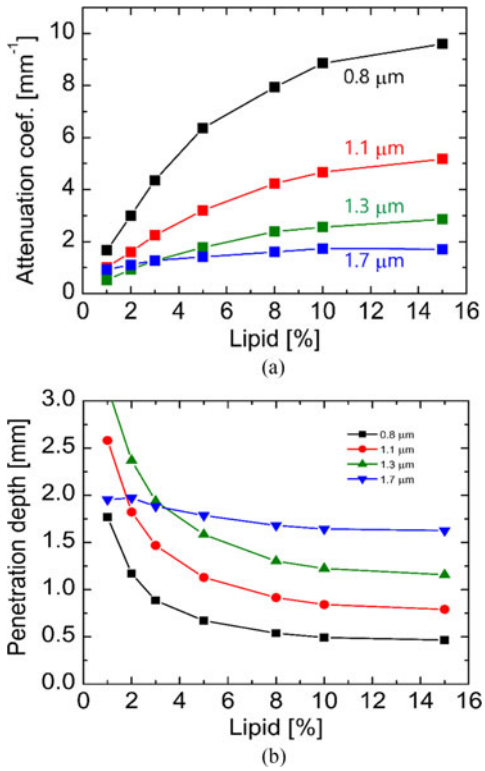

Fig. 9. (a) Obtained attenuation coefficient and (b) penetration depth as functions of wavelength and lipid concentration.

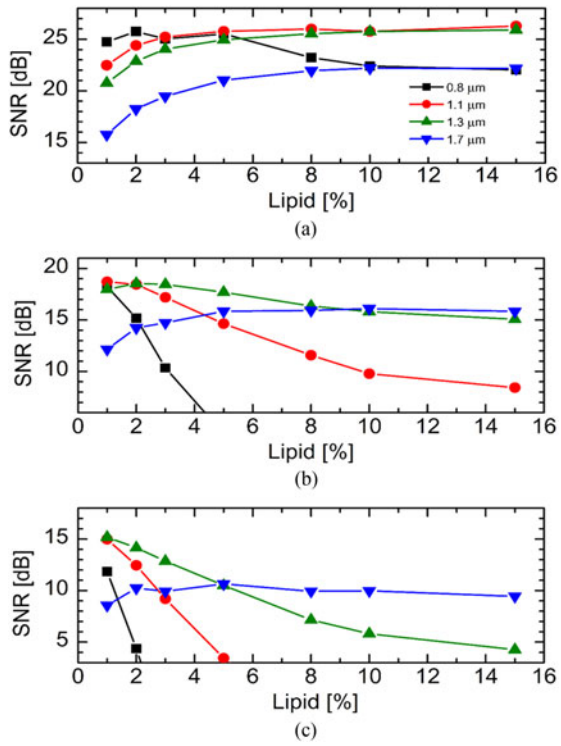

Fig. 10. Variation of contrast (SNR) as the functions of wavelength and lipid concentration. (a) Imaging depth: 0.2 mm. (b) Imaging depth: 0.6 mm. (c)Imaging depth: 1.00 mm.

for the measurement in the phantom with high lipid density, the attenuation line obtained from the single scattering model deviated greatly from the measured results at $\lambda = 1.7$ μm. This suggests that the actual noise floor was increased by multiple scattering in OCT imaging. At $\lambda = 1.7$ μm, the effect of multiple scattering at a deep part in the sample was not observed.

Figure 9(b) shows the wavelength dependence of the penetration depth, obtained with the single scattering model. For 1.7 μm OCT imaging, in the sample with low lipid density, the image contrast was low and the imaging depth was short compared to those at $\lambda = 1.1$ and 1.3 μm, owing to the small scattering coefficient and the effect of water absorption. As the lipid density increased, the imaging depth decreased at $\lambda = 0.8$–1.3 μm. On the other hand, at $\lambda = 1.7$ μm, the imaging depth was almost constant and independent of the lipid density. In the high-scattering phantom, which had a lipid density of 5–15%, the deepest penetration depth was achieved at $\lambda = 1.7$ μm, which is consistent with previous findings [29], [30].

Using the signal attenuation line obtained with the single scattering model, SNRs of OCT images at depths of 0.2, 0.6, and 1.0 mm from the surface were obtained (Fig. 10). For the OCT imaging around the sample surface, the image contrast was degraded in the low-scattering sample at $\lambda = 1.7$ μm. On the other hand, in the high-scattering sample, the same or larger imaging contrast was achieved at the deep part by use of $\lambda = 1.7$ μm, compared to those at $\lambda = 1.3$ μm. In order to obtain a high-contrast OCT image at a deep part, the advantage of using $\lambda = 1.7$ μm was enhanced as the scattering coefficient increased.

Here we will discuss the results of this section in terms of biological imaging. The magnitude of the scattering coefficient of the lipid mixture (10% lipid concentration) was ~2/mm at $\lambda = 1.6$ μm [30]. This magnitude is almost the same as those of brain and skin tissue at $\lambda = 1.6$–1.7 μm, which are 1–3/mm [31], [32]. In the lipid mixture solution prepared in this work, the D_2O was added so that the volume ratio of H_2O reached a value of 70%, which is the same as the value in actual brain and skin tissue [26], [27]. As a result, the OCT imaging characteristics obtained in the 70% lipid mixture solution were close to those obtained for the actual brain and skin tissues. In Fig. 9, the highest penetration depth was obtained at $\lambda = 1.7$ μm. So it is considered that the deepest imaging can be achieved for actual brain and skin tissue when we use a 1.7 μm OCT system. On the other hand, considering the results in Fig. 10(b), OCT systems operating at $\lambda = 0.8$–1.0 μm are effective for achieving deep imaging in low-scattering samples.

In our previous work, we examined the impact of light scattering, water absorption, and chromatic dispersion for deep-tissue OCT imaging at 1.7 μm wavelength range [33]. The lipid phantom used in this section was used as the quantitative sample.

As the results, the degradation of axial resolution was observed inside the lipid phantom. When the lipid density was increased, the axial resolution did not change. It means that the scattering does not cause the chromatic dispersion. On the other hand, when the thickness of the sample was increased, the axial resolution and SNR were both degraded. It was confirmed that the degradation of axial resolution was mainly caused by the chromatic dispersion of water. It was also observed that the optical spectra suffered the absorption of water. As the thickness of the sample was increased, the magnitude of absorption was increased and the spectral shape of irradiated beam was slightly changed. The effect of water absorption caused the degradation of SNR.

The magnitude of chromatic dispersion of water takes the minimum around 1.0 μm range, and it increases as the wavelength increases. As the results, the effect of chromatic dispersion inside the sample is increased as the wavelength is increased.

Although the magnitude of chromatic dispersion inside the sample is large at $\lambda = 1.7$ μm, we confirmed that it could be compensated by the conventional dispersion compensation with glass materials. As the results, the high axial resolution close to the theoretical one was achieved for the deep-tissue OCT imaging at $\lambda = 1.7$ μm.

IV. UHR-OCT Imaging of Rat Lung

In this section, taking account of the results in the previous section, we describe experiments using the developed OCT system for biomedical imaging.

Lung imaging is important for lung physiology and pathology. For example, accurate measurement of alveolar volume under different environments or clinical conditions can provide information about the stability, interdependence, and mechanism of alveolar collapse and reopening specifically under mechanical ventilation or conditions of atelectasis recovery.

Recently, OCT has been gaining credibility as a pulmonary imaging tool [34]–[37]. OCT is a promising advanced diagnostic technology for real-time imaging of abnormalities in the chest for assessing the degree of fibrosis or inflammation in seriously ill patients with pulmonary diseases, without the need for lung resection.

The first OCT imaging of the lung was reported by groups at MIT and Massachusetts General Hospital (MGH) [38], [39]. Following this, Tsuboi *et al.* demonstrated OCT imaging of samples extracted from central type lung cancers [40]. Hanna *et al.* reported OCT imaging of histological lung tissue [41]. Recently, three-dimensional OCT imaging of the alveolar structure of a ventilated rabbit lung was demonstrated using a Fourier-domain OCT system [42]–[44]. Recently, fiber needle probes have been actively investigated for in vivo OCT imaging of lung tissue [45]–[47].

Recently, we demonstrated UHR time domain OCT imaging of isolated rat lungs using SC in the 800 nm, 1060 nm, and 1300 nm wavelength ranges [15]. Index matching using phosphate buffered saline (PBS) was demonstrated, and fine structures of the airway tissue and lung tissue were clearly observed by cross-sectional imaging. As a result, the finest structures of lung tissue were observed at a wavelength of 800 nm, and the highest contrast was achieved at a wavelength of 1060 nm. These results are consistent with those in the previous section.

Chronic obstructive pulmonary disease (COPD) has recently been identified as one of the leading causes of morbidity and mortality worldwide. The chronic inflammatory changes characteristic of COPD are found in the airways, lung parenchyma, and pulmonary vasculature [48]. The major sites of obstruction in COPD are small airways (<2 mm in diameter). The narrowing and disappearance of small conducting airways before the onset of emphysematous destruction, such as centrilobular emphysema or panlobular emphysema, is reported to increase peripheral airway resistance in COPD [49]. OCT is expected to offer clinical advantages for the detection of these pathological and structural changes to track disease progression. To investigate this, we used a dexamethasone-treated rat, which is a model of a developmental defect rather than of emphysema; however, the results showed a pathological pattern of enlarged distal air spaces with reduced alveolar number (alveolar simplification), similar to COPD [50], [51].

Owing to the development of medical imaging technologies such as computed tomography (CT), three-dimensional image processing techniques have advanced greatly. In the field of OCT, we can now obtain large 3D data, and it is also important to process and analyze the observed 3D image data. Meissner *et al.* demonstrated the feasibility of the segmentation and quantification of alveoli with OCT [52]. Pagnozzi *et al.* demonstrated the automated quantification of lung structure using OCT with a fiber needle probe [53].

In the work described in this section, we demonstrated three-dimensional OCT imaging and volume analysis of rat lung tissue. Formalin-fixed rat lungs and those filled with air or PBS were prepared as samples. For imaging, we mainly used UHR-TD-OCT systems operating in the 820 nm and 1060 nm wavelength regions. For the comparison, and especially 3D imaging, we also used a spectral domain (SD) OCT operating in the 930 nm wavelength region. We compared the observed OCT images and examined the wavelength dependence.

TABLE II
CHARACTERISTICS OF OCT SYSTEMS USED IN THIS WORK

System	Axial resolution [μm]	Lateral resolution [μm]	Sensitivity [dB]
820 nm TD-OCT	3.7	10.7	100
930 nm SD-OCT	7.0	8.0	105
1060 nm TD-OCT	4.6	10.1	104

For three-dimensional rendering and analysis, we utilized software that we developed, called NewVES, which is a 3D virtual endoscopy system using a fast software-based volume rendering technique [54]. Then, as the diseased samples, the lungs of dexamethasone-treated rats were examined. Using the NewVES, the volume of alveoli for each sample was estimated from the OCT images, and their variation was examined.

A. Methods and Materials

In this work, we used three OCT systems, operating in the 820 nm, 930 nm, and 1060 nm wavelength regions. For the 820 nm and 1060 nm regions, we used UHR-TD-OCT systems, shown in Fig. 6. The SC was generated using an ultrashort-pulse solid state laser and a single mode fiber, as shown in Figs. 1–3. For the 930 nm wavelength region, we used a commercially available SD-OCT system (Thorlab, Callisto). A super-luminescent diode (SLD) was used as the broadband light source. The axial resolution was 7.0 μm in air, and the lateral resolution was 8 μm. The sensitivity was 105 dB for the irradiation power of 1.5 mW at the sample. The imaging speed was 1,200 A scans per second. The characteristics of the OCT systems used are summarized in Table II.

We demonstrated OCT imaging of rat lung tissues. As the samples, Sprague-Dawley (SD) rats (10 weeks of age, obtained from Japan SLC, Shizuoka, Japan) were used for all experiments. The rats were maintained in a room under conventional conditions and were provided with food and water ad libitum. All procedures were performed in accordance with the Animal Experimental Guides of Nagoya University Graduate School of Medicine. Rats were sacrificed by exsanguination from the abdominal aorta under anesthesia. The lungs, with cannulated trachea, were removed and inflated. In this work, the inflation pressure was fixed at 10 cmH_2O for all samples.

B. Results and Discussion

1) Normal Rat Lung Tissue: First, we demonstrated the OCT imaging of normal rat lung tissue. Fig. 11 shows the images observed in the 820 and 1060 nm wavelength regions. Fig. 11(a, b) shows cross-sectional OCT images for the normal rat lung tissue inflated with air. The inflation pressure was set at 10 cmH_2O. Owing to the large difference in refractive index between the air and lung tissue, the shapes of the alveoli changed due to total or multiple reflections at the alveolar wall [55]. One or two alveoli just beneath the visceral pleura were observed. We examined four samples, and the similar images were observed in all samples.

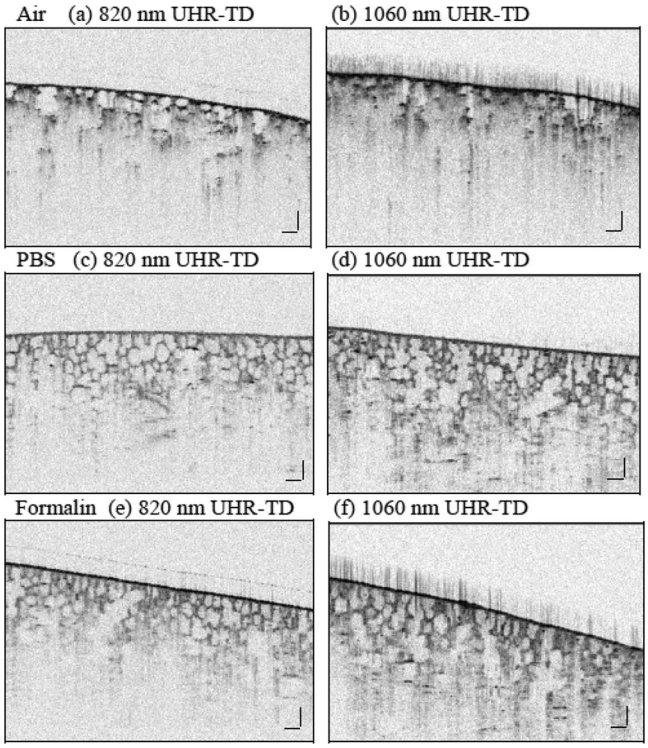

Fig. 11. Cross-sectional OCT images of normal rat lung tissues (a,b) inflated with air, instilled with (c, d) PBS, or (e, f) formalin. The inflation pressure was set at 10 cmH_2O. The cross-sectional images were observed with UHR-TD-OCT at (a, c, e) 820 nm and (b, d, f) 1060 nm. The inflation pressure was fixed at 10 cmH_2O for all samples. The scale bars correspond to a 100 μm length in the tissue.

Figure 11(c, d) shows the cross-sectional images when the lung tissue was instilled with PBS in place of air. The instillation pressure was set at 10 cmH_2O. Owing to the index matching with PBS, the alveoli were observed clearly with high resolution. Three to five alveoli just beneath the visceral pleura were observed clearly. Similar to the previous work, the finest images were observed in the 820 nm wavelength region, and deeper images with high contrast were observed in the 1060 nm wavelength region. Using SD-OCT in the 930 nm wavelength region, similar images to those in the 1060 nm wavelength region were observed.

Figure 11(e, f) shows observed cross-sectional images of formalin-fixed rat lung tissues. Clear images similar to those observed for the PBS-instilled lung tissue were observed for all wavelengths.

Figure 12(a) and (b) show enlarged 3D-UHR-OCT images of a formalin fixed rat lung inflated to a pressure of 20 cmH_2O. The UHR-TD-OCT at 820 nm wavelength region was used for imaging. The shapes of the alveolar sac and alveoli were clearly observed, and the interalveolar septa were also clearly observed. From the animation (Visualization 2), we could see the variation of the shape from alveoli to sac as the imaging depth was increased.

Figure 13 shows a hematoxylin and eosin-stained histological image of the formalin-fixed normal rat lung tissue. The histological sample was made from the same sample used in OCT imaging. We can see that the size and shape of the alveoli and alveolar sac were almost the same in both the OCT images and the histological ones.

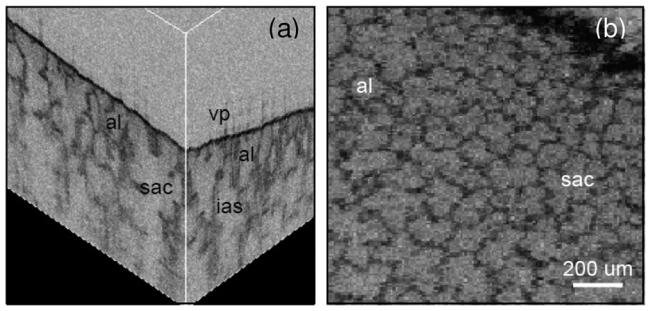

Fig. 12. Enlarged 3D UHR-OCT images of formalin fixed rat lung, showing (a) 3D (Visualization 1) and (b) *en face* images (Visualization 2). The inflation pressure was 20 cmH_2O. al: alveolus; ias: interalveolar septum; sac: alveolar sac; vp: visceral pleura.

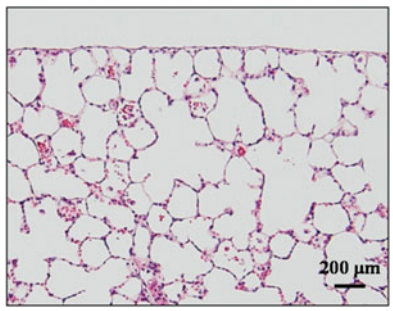

Fig. 13. Hematoxylin and eosin-stained histological image of the formalin-fixed normal rat lung tissue.

Using the SD-OCT system, since the imaging speed was fast, we could observe the 3D OCT image of biomedical samples smoothly. In this work, each 3D image was taken within 4 min for SD-OCT. The 3D image was constructed using the NewVES software, which is specially designed software for virtual endoscopy systems developed by Mori [54]. 3D representation using a volume rendering technique was demonstrated. In addition to the noise elimination and contrast enhancement, it has many functions for image processing, such as division and coupling of images, and estimation of length and volume. Using this software, we can view any part of the 3D imaging data from arbitrary angles.

Figure 14 shows the observed 3D images and 3D representation obtained using NewVES. Clear and high resolution 3D images were obtained, and detailed structures of the lung tissues were observed. For the formalin-fixed samples, the 3D images were also taken with UHR-TD-OCT at two wavelengths. Since it took a long time to achieve the 3D images, the imaging area was limited to 1/4 of that for SD-OCT imaging. Similar but more precise images were observed with ultrahigh resolution.

Next, we tried to estimate the volume of an alveolus for each lung sample using the analysis process in NewVES. Four samples of normal rat lung were used as the control. Each alveolus was separated automatically by signal processing, and the volumes of alveolus were estimated (Visualization 4). The average volume and standard deviation were estimated for 90 alveoli in each lung tissue sample.

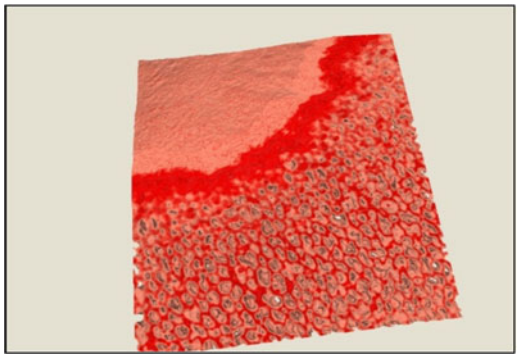

Fig. 14. 3D OCT image of normal rat lung instilled with 10% formalin (Visualization 3). The inflation pressure was 10 cmH_2O.The NewVES software was used for 3D image construction. The volume estimation process with NewVES is also shown in Visualization 4.

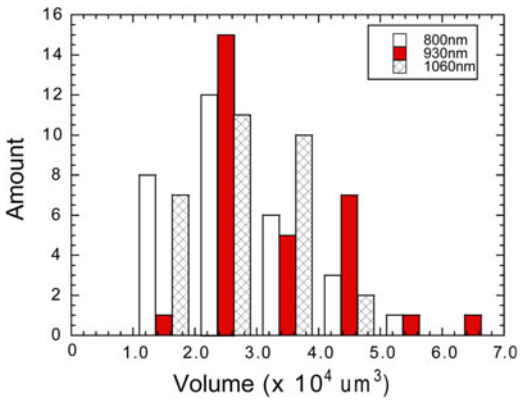

Fig. 15. Distribution of estimated alveolar volume of formalin-fixed normal rat lung samples with pressures of 10 cmH_2O using OCT systems operating at wavelengths of 820, 930, and 1060 nm.

TABLE III
ESTIMATED ALVEOLAR VOLUME OF FORMALIN-FIXED NORMAL RAT LUNG SAMPLES OBSERVED WITH OCT SYSTEMS IN 3 WAVELENGTH REGIONS

	820 nm	930 nm	1060 nm
Averaged volume [μm^3]	3.3×10^4	2.7×10^4	2.8×10^4
Standard deviation [μm^3]	1.2×10^4	0.88×10^4	1.0×10^4

Figure 15 shows the distribution of estimated alveolar volume observed with 3 OCT systems. Formalin-fixed normal rat lungs were used as the samples. Almost the same places were observed for each OCT system. The estimated data are summarized in Table III. Similar values were achieved for all 3 OCT systems, and reliable repeatability was confirmed. The average values of alveolar volume were 2.7×10^4 to 3.3×10^4 μm^3, and the standard deviation was 0.88×10^4 to 1.2×10^4. The estimated magnitudes were almost in agreement with the previously reported ones [56]–[58].

2) Rat Lungs With Emphysema-Like Morphological Changes: Next, in order to discuss the effectiveness of OCT for imaging lungs with COPD, we used dexamethasone-treated rat lungs. Newborn Sprague-Dawley (SD) rats were injected with dexamethasone (0.25 μg/day) subcutaneously from day 4 until day 13 to induce emphysema-like morphological changes, as previously described [50], [51]. Ten weeks after the last injection of dexamethasone, the rats were examined for histological changes [51]. The lungs, with cannulated trachea, were removed and then inflated with air and instilled with PBS or 10% formalin to a pressure of 10 cmH_2O.

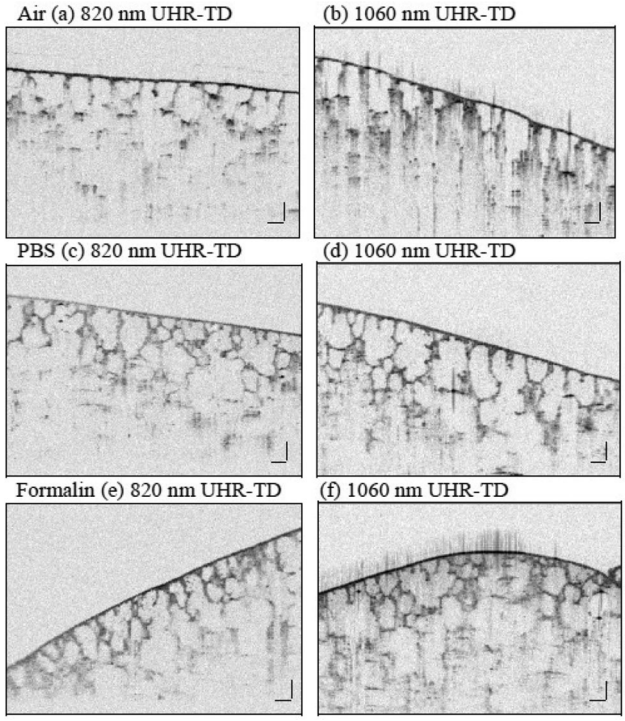

Fig. 16. Cross-sectional OCT images of dexamethasone-treated rat lung tissues inflated with (a, b) air, instilled with (c, d) PBS, or (e, f) formalin. The inflation pressure was set at 10 cmH_2O for all samples. The cross-sectional images were observed with UHR-TD-OCT at (a, c, e) 820 nm, and (b, d, f) 1060 nm. The scale bars correspond to a 100 μm length in the tissue.

Figure 16 shows cross-sectional OCT images of the dexamethasone-treated rat lungs. Compared with the lung of the normal rat, the OCT images of the lung of the dexamethasone-treated rat showed markedly different alveolar morphology, with fewer, larger alveoli. These histological and structural changes observed in the UHR-OCT images are in good agreement with those observed using a standard hematoxylin and eosin staining method used in histology. Among the three inflation conditions, the clearest OCT images were observed with PBS inflation. We also observed fine OCT images of the lung in the case of 10% formalin, since the index matching between the lung tissue and the 10% formalin was similar to that between the lung tissue and PBS. Emphysema- like morphological changes were clearly observed in the dexamethasone-treated rat lung.

It is interesting to note that since the number of alveolar walls was smaller than that in normal lung tissue, deeper images were acquired in the diseased lungs, even those inflated with air.

Figure 17 shows the observed hematoxylin and eosin-stained histological images of dexamethasone-treated rat lung. We can clearly see that the number of alveolar walls was less, and larger alveoli were observed. The histological images were almost in agreement with the observed OCT images.

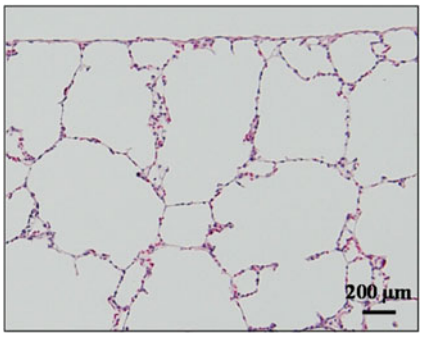

Fig. 17. Hematoxylin and eosin-stained histological image of the formalin fixed dexamethasone-treated rat lung.

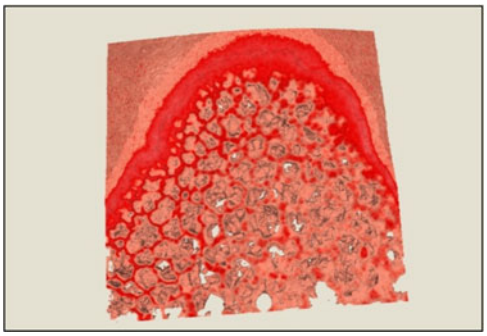

Fig. 18. 3D OCT images of dexamethasone-treated rat lung inflated with formalin. The corresponding 3D images are also shown in Visualization 5 and Visualization 6.

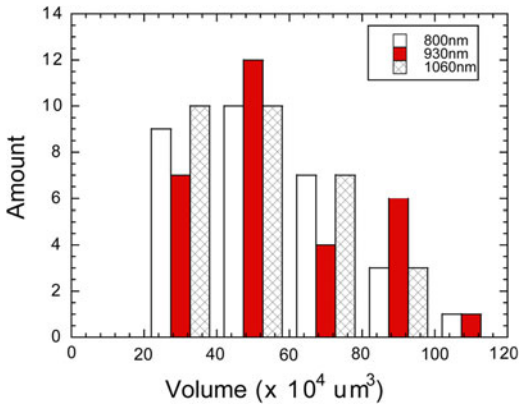

Fig. 19. Distribution of estimated alveolar volume of formalin-fixed dexamethasone-treated rat lung samples with pressures of 10 cmH_2O using OCT systems operating at wavelengths of 800, 930, and 1060 nm.

Figure 18 shows the observed 3D images and 3D representation obtained with NewVES. 3D structural changes of lung tissue were clearly represented. Using one of the functions of NewVES, we can see anywhere inside the 3D image data.

Figure 19 shows the distribution of estimated alveolar volume for dexamethasone-treated rat lungs. The formalin-fixed rat lungs were used as the samples, and three OCT systems were used for the measurement. The same process used for Figure 15 was applied for the volume estimation. The estimated data are summarized in Table IV. Close values were achieved for all three OCT systems, thus confirming reliable repeatability. For the dexamethasone-treated rat lungs, the average values of alveolar volume were 51.8×10^4 to 56.8×10^4 μm^3, and the standard deviation was 19.5×10^4 to 23.5×10^4. The expansion ratios of the alveolar volume relative to that of the normal rat lung were 16–21. We confirmed the structural changes quantitatively by non-destructive OCT measurement.

TABLE IV
ESTIMATED ALVEOLAR VOLUME OF FORMALIN-FIXED DEXAMETHASONE-TREATED RAT LUNG SAMPLES OBSERVED WITH OCT SYSTEMS IN THREE WAVELENGTH REGIONS

	820 nm	930 nm	1060 nm
Averaged volume [μm^3]	53.3×10^4	56.8×10^4	51.8×10^4
Standard deviation [μm^3]	22.3×10^4	23.5×10^4	19.5×10^4
Expansion ratio	16	21	19

V. 1.7 μM OCT AND OCM

In this section, we discuss OCT imaging at $\lambda = 1.7$ μm. At the present time, OCT systems operating in the $\lambda = 0.8$–1.3 μm region are widely used for not only clinical medicine but also fundamental biological and medical research studies, such as brain science studies [59]–[62]. Although OCT provides excellent imaging capabilities, the penetration depth in turbid tissues has been limited by signal attenuation due to multiple scattering and water absorption.

Since the scattering magnitude decreases as the wavelength is increased, recently, the use of a wavelength region longer than 1.3 μm has been proposed in order to increase the penetration depth [13], [16], [29], [30], [63]. These investigations revealed that the 1.7 μm wavelength band is a promising choice for enhancing the penetration depth in turbid tissue, because there is a local minimum of water absorption there.

In the previous section, we investigated the wavelength dependence of OCT imaging quantitatively using biological phantoms. As a result, we confirmed that the 1.7 μm range is useful for deep OCT imaging in highly scattering samples.

Previously, we successfully demonstrated deep-penetration UHR-TD-OCT imaging using an SC generated in the 1.7 μm range [13], [16], [63]. Recently, the SD-OCT and SS-OCT at 1.7 μm have been reported [64], [65]. The ability to image hippocampal structures in a mouse brain with enhanced penetration depth compared with a 1.3 μm OCT system was reported [65].

In this section, we present a full-range UHR-SD-OCT system developed using a 1.7 μm SC source for high-resolution deep tissue imaging [66].

As shown in Fig. 3, we have to use an extremely broadband SC to achieve a high axial resolution of $\sim$3 μm. Detecting such broadband light normally involves a sacrifice of the spectral resolution due to the finite pixel number of the detection camera in the spectrometer used in the SD-OCT system.

In this work, in order to overcome this issue, we employed a full-range OCT technique, which uses a phase modulation method [67]–[69].

Figure 20 shows the configuration of our developed UHR-SD-OCT operating in the $\lambda = 1.7$ μm range. An Er-doped fiber laser-based SC at 1.7 μm was used as the light source. The generated SC was introduced into a fiber Michelson interferometer. For

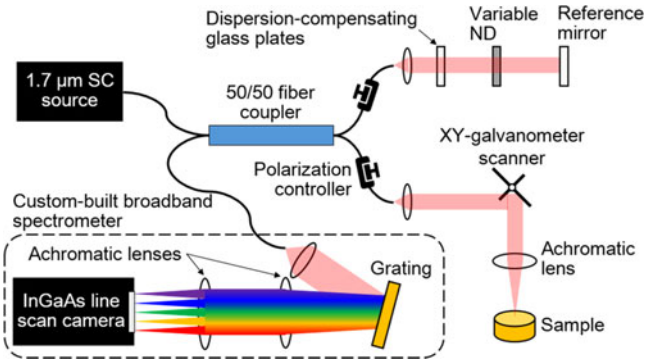

Fig. 20. Configuration of UHR-SD-OCT at $\lambda = 1.7$ μm.

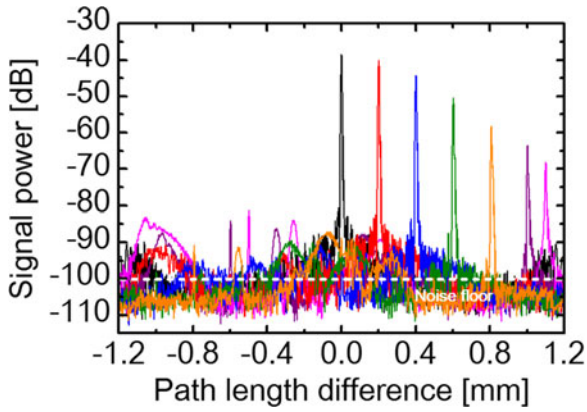

Fig. 21. Sensitivity roll-off of UHR-SD-OCT at $\lambda = 1.7$ μm.

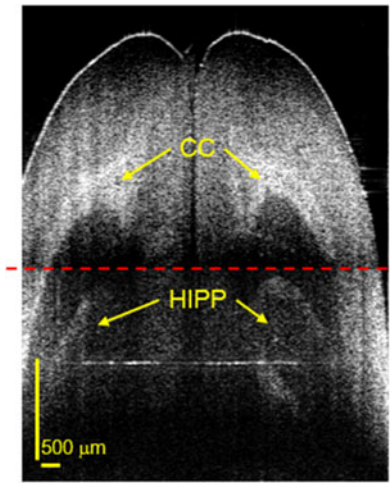

Fig. 22. Observed OCT image of mouse brain. CC, corpus callosum; HIPP, hippocampus.

the reference arm, a variable ND and dispersion compensation glass were used to achieve the highest-performance OCT imaging. For the sample arm, an x-y galvanometer mirror and an achromatic lens were used for beam scanning. The focal length of the achromatic lens was 30 mm. At the galvanometer mirror, in order to increase the imaging range, an offset was added to the collimated beam to demonstrate the full-range OCT imaging [69]–[71]. For the detection system, a high-speed polychromator was developed using a high-speed InGaAs line scan camera (Goodrich SU1024LDH-2.2RT-0250/LC), diffraction grating, and achromatic lenses. Zmax software was used for designing the polychromator. The wavelength resolution was 1 nm, and the detection range was 1.4–2.0 μm.

The imaging system was constructed with LabView. The line-rate of the camera was 47 kHz, and the imaging speed was 83 frames/s.

Owing to the offset on the x-axis galvanometer scanner, a constant phase shift was added to the adjacent A-scans during the B-scan. The obtained cross-sectional data was Fourier transformed along the transverse scanning direction (B-scan direction). Because each A-scan had a constant phase shift, the signal spectrum in the spatial frequency domain was shifted to both positive and negative frequency regions. Therefore, by cutting out one of the signal spectra and applying an inverse Fourier transformation along the B-scan direction, complex interference spectra were achieved. Finally, a full-range OCT image, which is an image constructed using only a primary OCT signal, was generated by the Fourier transform of the complex interferograms for each A-scan.

Figure 21 shows the sensitivity roll-off of the developed full-range SD-OCT. A silver mirror was used as the sample, and an ND filter was inserted to avoid saturation of the detector. As shown in Fig. 21, the ghost image was well-suppressed, and the suppression ratio was $\sim$40 dB in the whole region. There were small peaks at depths around -0.2 to -0.8 mm, which were considered to be caused by the residual dispersion mismatch and the non-ideal spectral shape. The average axial resolution was 4.9 um in air, and 3.6 um in tissue under the assumption of a refractive index of 1.38. The measured sensitivity roll-off was -10 dB/0.5 mm. We confirmed that it was possible to achieve a full-range OCT image with an imaging area of 9.6 mm (X) $\times$ 6.8 mm (Y).

Next, we demonstrated the OCT imaging of biological samples using the developed OCT system. Fig. 22 shows the full-range OCT images of the mouse brain. The brain is a highly scattering sample with low water absorption, and the 1.7 μm range is expected to be useful for imaging of the brain tissue. 3D imaging was demonstrated thanks to the fast imaging speed of the SD-OCT system. The corpus callosum (CC) and hippocampus (HIPP), which are characteristic structures in brain tissue, were clearly visualized.

Figure 23 shows *en face* slices of the observed rat mouse brain at depths of 0.9 and 1.6 mm. The axisymmetric structures of CC and HIPP were clearly observed even at the deep region.

In OCT, since a long focal length is used for cross-sectional imaging, the lateral resolution is generally $\sim$10 μm. Using a high-NA lens, although the depth of focus is shortened, we can achieve high-lateral-resolution imaging at a fixed depth. This scheme is known as optical coherence microscopy (OCM) [72].

OCM is an imaging modality based on OCT and confocal microscopy, which realizes high spatial resolution in three dimensions. The combination of OCT and confocal detection schemes also helps to improve the image contrast by the enhanced rejection capability of signals from out-of-focus. So far, OCM techniques have been successfully applied to visualize small details in various biological samples, such as myelin fibers and cerebral cortex in brain specimens [73]–[76]. One of the current critical issues with OCM is the shallow imaging depth, like that in the

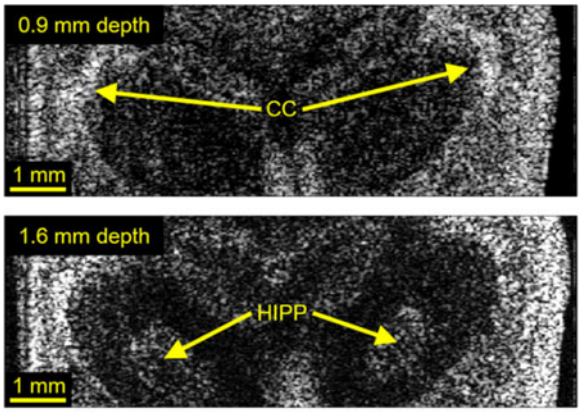

Fig. 23. Reconstructed *en face* images of the mouse brain at depths of 0.9 and 1.6 mm.

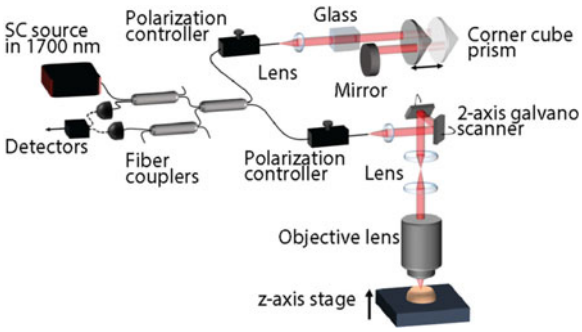

Fig. 24. Configuration of developed OCM system operating at $\lambda = 1.7$ μm.

case of OCT. Since OCM provides imaging capabilities with high spatial resolution in three dimensions, an improvement of the imaging depth in OCM would be greatly beneficial to a wide variety of biological investigations, such as brain studies.

In this work, we developed an UHR-OCM system operating at 1.7 μm. This is the first OCM system developed for operation at this wavelength [77].

Figure 24 shows the configuration of the developed OCM system operating at $\lambda = 1.7$ μm. A high-NA objective lens working in the 1.7 μm range was used in the sample arm. The focal length was short but we could obtain high-resolution *en face* images. The interferometer consisted of broadband fiber couplers working at 1.7 μm. Extended InGaAs photodiodes were used for the detector, and interference signals were obtained at the balanced detector. A corner cube prism was used to scan the length of the reference arm. With this OCM system, we achieved both high lateral and axial resolutions.

Figure 25 shows the observed OCM image of a single polystyrene bead with a diameter of 200 nm. From this image, the lateral resolution was estimated to be 1.3 μm, and the axial resolution was 2.8 μm. Therefore, we realized a high-resolution OCM imaging system.

Figure 26 shows the *en face* image of an observed pig thyroid gland. The imaging depth was 150 μm from the surface. The OCM system clearly visualized follicles and a single layer of epithelial cells, which are characteristic structures of pig thyroid gland.

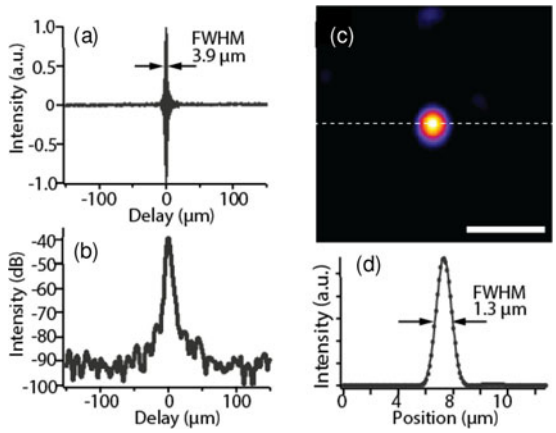

Fig. 25. (a) Interference signal obtained with the developed OCM, (b) logarithmically demodulated signal, (c) *en face* OCM image of 200 nm single polystyrene bead and (d) its intensity profile.

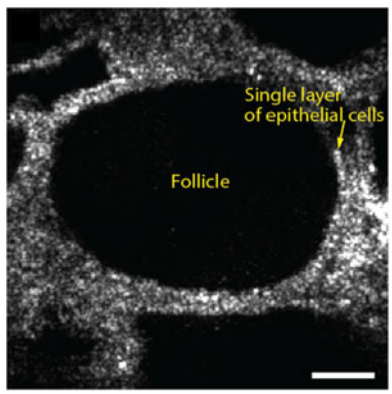

Fig. 26. OCM image of a pig thyroid gland at a depth of 150 μm.

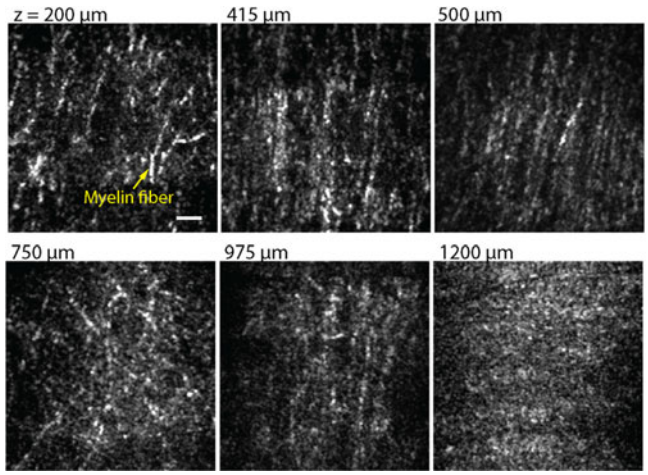

Fig. 27. *En face* OCM images of mouse brain at several different depths. Scale bar corresponds to 20 μm.

Then, we demonstrated the *en face* OCM imaging of a fixed mouse brain at various imaging depths, as shown in Fig. 27.

Fiber-like structures were clearly observed up to a depth of 0.95 mm. Fiber-like structures were considered to be myelin fibers. At a depth of 1.2 mm, no fiber-like structures were observed. It is considered that this image represents the structures

of white matter, or alveus hippocampi, in the mouse brain. We also demonstrated deep *en face* imaging of a pig thyroid gland. From these results, we confirmed that we can demonstrate high-resolution deep imaging in turbid tissues using 1.7 μm OCM.

VI. Conclusion

In this work, we investigated the wavelength dependence of ultrahigh-resolution (UHR) optical coherence tomography (OCT) using a supercontinuum (SC) for biomedical imaging. First, we explained the generation of a wideband SC for OCT. We developed a Gaussian-like, high-power, low-noise SC using ultrashort pulse lasers and highly nonlinear fibers. We prepared SC and OCT systems operating in four different wavelength ranges, and examined the wavelength dependence of OCT imaging. In this work, we prepared biological phantoms using lipid, and we quantitatively examined the dependence of OCT imaging on the wavelength and scattering magnitude, in particular, the attenuation coefficient, penetration depth, and image contrast. As a result, it was confirmed that $\lambda = 1.7$ μm is suitable for deep imaging in turbid tissue having a large scattering coefficient. For low-scattering samples, the wavelength range of $\lambda = 0.8$–1.0 μm is effective for deep imaging.

Then, considering the results of wavelength dependence, biomedical imaging of animal samples was demonstrated. First, 3D cross-sectional imaging of rat lung was demonstrated using 0.8–1.0 μm OCT systems. Clear images of the alveoli were observed due to the index matching effect of the liquid used for inflation. The precise structures of lung tissue was observed with UHR-OCT. 3D image processing software called NewVES was applied, and clear 3D images were obtained. Emphysema-like morphological changes were clearly observed in the lungs of dexamethasone-treated rats. The volumes of alveoli were estimated for formalin-fixed samples using NewVES. This is the first report of non-destructive estimation of alveolar volume.

Next, we developed a UHR-spectral domain (SD) OCT system operating at $\lambda = 1.7$ μm for deep 3D imaging of turbid tissue. The full-range technique was used to enlarge the imaging range. A high axial resolution of 3 μm in tissue was achieved with a high-power SC source. A fast imaging speed of 83 frames/s was achieved using a line-scan camera. Deep OCT imaging inside mouse brain was achieved, and part of the hippocampus was observed at a depth of 1.6 mm.

Finally, an optical coherence microscopy (OCM) system operating at $\lambda = 1.7$ μm was developed for the first time. A fiber-laser-based SC source, a high-numerical-aperture lens, and a time-domain interferometer were used for this OCM system. The lateral resolution was 1.3 μm, and the axial resolution was 2.8 μm. The precise structures of mouse brain were observed successfully at a depth of 1.2 mm.

References

[1] D. Huang *et al.*, "Optical coherence tomography," *Sci.*, vol. 254, pp. 1178–1181, 1991.

[2] B. E. Bouma and G. J. Tearney, *Handbook of Optical Coherence Tomography*, New York, NJ, USA: Marcel Dekker, 2002.

[3] W. Drexler and J. G. Fujimoto, *Optical Coherence Tomography—Technology and Applications*, 2nd ed., Bazel, Switzerland: Springer, 2015.

[4] I. Hartl *et al.*, "Ultrahigh-resolution optical coherence tomography using continuum generation in an air-silica microstructure optical fiber," *Opt. Lett.*, vol. 26, pp. 608–610, 2001.

[5] B. Povazay *et al.*, "Submicrometer axial resolution optical coherence tomography," *Opt. Lett.*, vol. 27, p. 1800, 2002.

[6] R. R. Alfano, *The Supercontinuum Laser Source—Fundamentals With Updated References*, 2nd ed., New York, NY, USA: Springer, 2006.

[7] J. M. Dudley and J. R. Taylor, *Supercontinuum Generation in Optical Fibers*, New York, NY, USA: Cambridge University Press, 2010.

[8] Z. Zhi, J. Qin, L. An, and K. Wang, "Supercontinuum light source enables in vivo optical microangiography of capillary vessels within tissue beds," *Opt. Lett.*, vol. 36, p. 3169, 2011.

[9] F. E. Robles, C. Wilson, G. Grant, and A. Wax, "Molecular imaging true-colour spectroscopic optical coherence tomography," *Nat. Photon.*, vol. 5, p. 744, 2011.

[10] W. Yuan *et al.*, "Optimal operational conditions for supercontinuum-based ultrahigh-resolution endoscopic OCT imaging," *Opt. Lett.*, vol. 41, p. 250, 2016.

[11] N. Nishizawa, Y. Chen, P. Hsiung, E. P. Ippen, and J. G. Fujimoto, "Real-time, ultrahigh-resolution, optical coherence tomography with an all-fiber, femtosecond fiber laser continuum at 1.5 mm," *Opt. Lett.*, vol. 29, p. 2846, 2004.

[12] M. Nishiura *et al.*, "In vivo ultrahigh-resolution ophthalmic optical coherence tomography using Gaussian-shaped supercontinuum," *Japanese J. Appl. Phys.*, vol. 49, 2010, Art. no. 012701.

[13] S. Ishida and N. Nishizawa, "Quantitative comparison of contrast and imaging depth of ultrahigh-resolution optical coherence tomography images in 800-1700 nm wavelength region," *Biomed. Opt. Express*, vol. 3, p. 282, 2012.

[14] S. Ishida and N. Nishizawa, "Ex-vivo imaging of thyroid gland using ultrahigh-resolution optical coherence tomography at wavelength from 800 to 1700 nm," *Japanese J. Appl. Phys.*, vol. 51, 2012, Art. no. 030203.

[15] S. Ishida *et al.*, "Observation of fine lung structure by ultrahigh-resolution optical coherence tomography using 800, 1060, and 1300 nm supercontinua," *Japanese J. Appl. Phys.*, vol. 51, 2012, Art. no. 047001.

[16] H. Kawagoe *et al.*, "Development of a high power supercontinuum source in the 1.7 mm wavelength region for highly penetrative ultrahigh-resolution optical coherence tomography," *Biomed. Opt. Express*, vol. 5, p. 932, 2014.

[17] J. M. Dudley, G. Genty, and S. Coen, "Supercontinuum generation in photonic crystal fiber," *Rev. Mod. Phys.*, vol. 78, p. 1135, 2006.

[18] T. Hori, N. Nishizawa, T. Goto, and M. Yoshida, "Experimental and numerical analysis of widely broadened supercontinuum generation in highly nonlinear dispersion shifted fiber with a femtosecond pulse," *J. Opt. Soc. Amer. B*, vol. 21, p. 1969, 2004.

[19] T. Hori, J. Takayanagi, N. Nishizawa, and T. Goto, "Flatly broadened, wideband and low noise supercontinuum generation in highly nonlinear hybrid fiber," *Opt. Express*, vol. 12, p. 317, 2004.

[20] J. Takayanagi and N. Nishizawa, "Generation of widely and flatly broadened, low-noise and high-coherence supercontinuum in all fiber system," *Japanese J. Appl. Phys.*, vol. 45, p. L441, 2006.

[21] N. Nishizawa and J. Takayanagi, "Octave spanning high-quality supercontinuum generation in all fiber system," *J. Opt. Soc. Amer. B*, vol. 24, p. 1786, 2007.

[22] Y. Nomura *et al.*, "Supercontinuum generation for ultrahigh-resolution optical coherence tomography at wavelength of 0.8 um using carbon nanotube fiber laser and similariton amplifier," *Appl. Phys. Express*, vol. 7, p. 122703, 2014.

[23] S. Bourquin, A. D. Aguirre, I. Hartl, P. Hsiung, T. H. Ko, and J. G. Fujimoto, "Ultrahigh resolution real time OCT imaging using a compact femtosecond Nd:Glass laser and nonlinear fiber," *Opt. Express*, vol. 11, p. 3290, 2003.

[24] B. W. Pogue and M. S. Patterson, "Review of tissue simulating phantoms for optical spectroscopy, imaging and dosimetry," *J. Biomed. Opt.*, vol. 11, 2006, Art. no. 041102.

[25] S. T. Flock, S. L. Jacques, B. C. Wilson, W. M. Star, and M. J. C. van Gemert, "Optical properties of intralipid: A phantom medium of light propagation studies," *Lasers Surg. Med.*, vol. 12, p. 510, 1992.

[26] H. Neeb, V. Ermer, T. Stocker, and N. J. Shaha, "Fast quantitative mapping of absolute water content with full brain coverage," *Neuroimage*, vol. 42, p. 1094, 2008.

[27] N. Nakagawa, M. Matsumoto, and S. Sakai, "In vivo measurement of the water content in the dermis by confocal Raman spectroscopy," *Skin Res. Technol.*, vol. 16, p. 137, 2010.

[28] J. M. Schmitt, "Optical coherence tomography (OCT): A review," *IEEE J. Sel. Topics Quantum Electron.*, vol. 5, no. 4, pp. 1205–1215, Jul./Aug. 1999.

[29] U. Sharma, E. W. Chang, and S. H. Yun, "Long-wavelength optical coherence tomography at 1.7 um for enhanced imaging depth," *Opt. Express*, vol. 16, p. 19712, 2008.

[30] V. M. Kodach, J. Kalkman, D. J. Faber, and T. G. van Leeuwen, "Quantitative comparison of the OCT imaging depth at 13200 nm and 1600 nm," *Biomed. Opt. Express*, vol. 1, p. 176, 2010.

[31] L. Shi, L. A. Sordillo, A. R. Contreras, and R. Alfano, "Transmission in near-infrared optical windows for deep brain imaging," *J. Biophoton.*, vol. 9, p. 38, 2016.

[32] A. N. Bashkatov, E. A. Genina, V. I. Kochubey, and V. V. Tuchin, "Optical properties of human skin, subcutaneous and mucous tissues in the wavelength range from 400 to 2000 nm," *J. Phys. D: Appl. Phys.*, vol. 38, p. 2543, 2005.

[33] H. Kawagoe, M. Yamanaka, and N. Nishizawa, "Axial resolution and signal-to-noise ratio in deep-tissue imaging with 1.7-μm high-resolution optical coherence tomography with an ultrabroadband laser source," *J. Biomed. Opt.*, vol. 22, 2017, Art. no. 085002.

[34] H. O. Coxson *et al.*, "Airway wall thickness assessed using computed tomography and optical coherence tomography," *Amer. J. Respir. Crit. Care Med.*, vol. 177, pp. 1201–1206, 2008.

[35] S. Lam *et al.*, "In vivo optical coherence tomography imaging of preinvasive bronchial lesions," *Clin. Cancer Res.*, vol. 14, pp. 2006–2011, 2008.

[36] J. P. Williamson *et al.*, "Elastic properties of the central airways in obstructive lung diseases measured using anatomical optical coherence tomography," *Amer. J. Respir. Crit. Care Med.*, vol. 183, pp. 612–619, 2011.

[37] J. Jing, J. Zhang, A. C. Loy, B. J. F. Wong, and Z. Chen, "High-speed upper-airway imaging using full-range optical coherence tomography," *J. Biomed. Opt.*, vol. 17, p. 110507, 2012.

[38] S. A. Boppart, B. E. Bouma, C. Pitris, G. J. Tearney, J. G. Fujimoto, and M. E. Brezinski, "Forward-imaging instruments for optical coherence tomography," *Opt. Lett.*, vol. 22, pp. 1618–1620, 1997.

[39] C. Pitris, M. E. Brezinski, B. E. Bouma, G. J. Tearney, J. F. Southern, and J. G. Fujimoto, "High resolution imaging of the upper respiratory tract with optical coherence tomography—A feasibility study," *Amer. J. Respir. Crit. Care Med.*, vol. 157, pp. 1640–1644, 1998.

[40] M. Tsuboi *et al.*, "Optical coherence tomography in the diagnosis of bronchial lesions," *Lung Cancer*, vol. 49, pp. 387–394, 2005.

[41] N. Hanna *et al.*, "Two-dimensional and 3-dimensional optical coherence tomography imaging of the airway, lung, and pleura," *J. Thorac. Cardiovasc. Surg.*, vol. 129, pp. 615–622, 2005.

[42] A. Popp, M. Wendel, L. Knels, T. Koch, and E. Koch, "Imaging of the three-dimensional alveolar structure and the alveolar mechanics of a ventilated and perfused isolated rabbit lung with Fourier domain optical coherence tomography," *J. Biomed. Opt.*, vol. 11, 2006, Art. no. 014015.

[43] S. Meissner, L. Knels, and E. Koch, "Improved three-dimensional Fourier domain optical coherence tomography by index matching in alveolar structures," *J. Biomed. Opt.*, vol. 14, 2009, Art. no. 064037.

[44] J. Bickenbach *et al.*, "Comparison of two in vivo microscopy techniques to visualize alveolar mechanics," *J. Clin. Monit. Comput.*, vol. 23, pp. 323–332, 2009.

[45] B. C. Quirk, R. A. McLaughlin, A. Curatolo, R. W. Kirk, P. B. Noble, and D. D. Sampson, "In situ imaging of lung alveoli with an optical coherence tomography needle probe," *J. Biomed. Opt.*, vol. 16, 2011, Art. no. 036009.

[46] R. A. McLaughlin *et al.*, "Static and dynamic imaging of alveoli using optical coherence tomography needle probes," *J. Appl. Physiol.*, vol. 113, pp. 967–974, 2012.

[47] K. M. Tan, M. Shishkov, A. Chee, M. B. Applegate, B. E. Bouma, and M. J. Suter, "Flexible transbronchial optical frequency domain imaging smart needle for biopsy guidance," *Biomed. Opt. Express*, vol. 3, pp. 1947–1954, 2012.

[48] J. Vestbo *et al.*, "Global strategy for the diagnosis, management, and prevention of chronic obstructive pulmonary disease: GOLD executive summary," *Amer. J. Respir. Crit. Care Med.*, vol. 187, p. 347, 2013.

[49] J. E. McDonough *et al.*, "Small-airway obstruction and emphysema in chronic obstructive pulmonary disease," *New England J. Medicine*, vol. 365, p. 1567, 2011.

[50] D. Massaro, N. Teich, S. Maxwell, G. D. Massaro, and P. Whitney, "Postnatal development of alveoli. Regulation and evidence for a critical period in rats," *J. Clin. Invest.*, vol. 76, p. 1297, 1985.

[51] G. D. Massaro and D. Massaro, "Postnatal treatment with retinoic acid increases the number of pulmonary alveoli in rats," *Amer. J. Physiol.*, vol. 270, p. L305, 1996.

[52] S. Meissner, L. Knels, C. Schnabel, T. Koch, and E. Koch, "Three-dimensional Fourier domain optical coherence tomography in vivo imaging of alveolar tissue in the intact thorax using the parietal pleura as a window," *J. Biomed. Opt.*, vol. 15, 2010, Art. no. 016030.

[53] A. M. Pagnozzi, R. W. Kirk, B. F. Kennedy, D. D. Sampson, and R. A. McLaughlin, "Automated quantification of lung structures from optical coherence tomography images," *Biomed. Opt. Express*, vol. 4, p. 2383, 2013.

[54] K. Mori, Y. Suenaga, and J. Toriwaki, "Fast software-based volume rendering using multimedia instructions on PC platforms and its application to virtual endoscopy," in *Proceedings SPIE*, p. 111, 2003, vol. 5031.

[55] A. Golabchi, J. Faust, F. N. Golabchi, D. H. Brooks, A. Gouldstone, and C. A. DiMarzio, "Refractive errors and corrections for OCT images in an inflated lung phantom," *Biomed. Opt. Express*, vol. 3, pp. 1101–1109, 2012.

[56] L. N. Blanco, G. D. Massaro, and D. Massaro, "Alveolar dimensions and number: Developmental and hormonal regulation," *Amer. J. Physiol.*, vol. 257, pp. L240–L247, 1989.

[57] J. Knust, M. Ochs, H. J. G. Gundersen, and J. R. Nyengaard, "Stereological estimates of alveolar number and size and capillary length and surface area in mice lungs," *Anatomical Rec.*, vol. 292, pp. 113–122, 2009.

[58] H. Parameswaran, E. Bartolak-Suki, H. Hamakawa, A. Majumdar, P. G. Allen, and B. Suki, "Three-dimensional measurement of alveolar airspace volumes in normal and emphysematous lungs using micro-CT," *J. Appl. Physiol.*, vol. 107, pp. 583–592, 2009.

[59] K. Bizheva *et al.*, "Imaging ex vivo and in vitro brain morphology in animal models with ultrahigh resolution optical coherence tomography," *J. Biomed. Opt.*, vol. 9, p. 719, 2004.

[60] W. J. Choi and R. K. Wang, "Swept-source optical coherence tomography powered by a 1.3-μm vertical cavity surface emitting laser enables 2.3-mm-deep brain imaging in mice in vivo," *J. Biomed. Opt.*, vol. 20, p. 106004, 2015.

[61] E. Sattler, R. Kästle, and J. Welzel, "Optical coherence tomography in dermatology," *J. Biomed. Opt.,* vol. 18, 2013, Art. no. 061224.

[62] P. L. Hsiung *et al.*, "Ultrahigh-resolution and 3-dimensional optical coherence tomography ex vivo imaging of the large and small intestines," *Gastrointest. Endosc.*, vol. 62, p. 561, 2005.

[63] S. Ishida, N. Nishizawa, T. Ohta, and K. Itoh, "Ultrahigh-resolution optical coherence tomography in 1.7 μm region with fiber laser supercontinuum in low-water-absorption samples," *Appl. Phys. Express*, vol. 4, 2011, Art. no. 052501.

[64] M. Tanaka, M. Hirano, K. Murashima, H. Obi, R. Yamaguchi, and T. Hasegawa, "1.7-μm spectroscopic spectral-domain optical coherence tomography for imaging lipid distribution within blood vessel," *Opt. Express*, vol. 23, p. 6645, 2015.

[65] S. P. Chong *et al.*, "Noninvasive, in vivo imaging of subcortical mouse brain regions with 1.7 μm optical coherence tomography," *Opt. Lett.*, vol. 40, p. 4911, 2015.

[66] H. Kawagoe, M. Yamanaka, S. Makita, Y. Yasuno, and N. Nishizawa, "Full-range ultrahigh-resolution spectral-domain optical coherence tomography in 1.7 um wavelength region for deep-penetration and high-resolution imaging of turbid tissues," *Appl. Phys. Express*, vol. 9, p. 127002, 2016.

[67] M. Wojtkowski, A. Kowalczyk, R. Leitgeb, and A. F. Fercher, "Full range complex spectral optical coherence tomography technique in eye imaging," *Opt. Lett.*, vol. 27, p. 1415, 2002.

[68] Y. Yasuno, *et al.*, "Simultaneous B–M-mode scanning method for real-time full-range Fourier domain optical coherence tomography," *Appl. Opt.*, vol. 45, p. 1861, 2006.

[69] B. Baumann, M. Pircher, E. Götzinger, and C. K. Hitzenberger, "Full range complex spectral domain optical coherence tomography without additional phase shifters," *Opt. Express*, vol. 15, p. 13375, 2007.

[70] R. K. Wang, "In vivo full range complex Fourier domain optical coherence tomography," *Appl. Phys. Lett.*, vol. 90, 2007, Art. no. 054103.

[71] R. A. Leitgeb, R. Michaely, T. Lasser, and S. C. Sekhar, "Complex ambiguity-free Fourier domain optical coherence tomography through transverse scanning," *Opt. Lett.*, vol. 32, p. 3453, 2007.

[72] J. A. Izzat, M. R. Hee, and G. M. Owen, "Optical coherence microscopy in scattering media," *Opt. Lett.*, vol. 19, pp. 590–592, 1994.

[73] O. O. Ahsen *et al.*, "Swept source optical coherence microscopy using a 1310 nm VCSEL light source," *Opt. Express*, vol. 21, pp. 18021–18033, 2013.

[74] A. D. Aguirre *et al.*, "Cellular resolution ex vivo imaging of gastrointestinal tissues with optical coherence microscopy," *J. Biomed. Opt.*, vol. 15, 2010, Art. no. 016025.

[75] V. J. Srinivasan, H. Radhakrishnan, J. Y. Jiang, S. Barry, and A. E. Cable, "Optical coherence microscopy for deep tissue imaging of the cerebral cortex with intrinsic contrast," *Opt. Express*, vol. 20, pp. 2220–2239, 2012.
[76] M. J. Yadlowsly, J. M. Schmitt, and R. F. Bonner, "Multiple scattering in optical coherence microscopy," *Appl. Opt.*, vol. 34, pp. 5699–5707, 1995.
[77] M. Yamanaka, T. Teranishi, H. Kawagoe, and N. Nishizawa, "Optical coherence microscopy in 1700 nm spectral band for high-resolution label-free deep-tissue imaging," *Scientific Rep.*, vol. 6, p. 31715, 2016.

Norihiko Nishizawa (M'99) received the M.E. and the Ph.D. degrees in quantum engineering from Nagoya University, Nagoya, Japan, in 1993 and 1995, respectively.

In 1995, he became a Research Associate with Nagoya University, where he has been an Associate Professor with the Department of Quantum Engineering since 2005. In 2007, he became an Associate Professor with the Division of Advanced Science and Biotechnology, Osaka University, Osaka, Japan. Since 2012, he has been a Professor with the Department of Electronics, Nagoya University. His research interests include ultrashort pulse fiber lasers, optical frequency combs, and their applications for biomedical imaging.

Dr. Nishizawa is a Member of the Japan Society of Applied Physics, Optical Society of Japan, the Laser Society of Japan, and OSA.

Hiroyuki Kawagoe received the Ph.D. degree in quantum engineering from Nagoya University, Nagoya, Japan, in 2017. He was involved with the development of 1.7 μm optical coherence tomography for deep-tissue imaging.

Following this, he joined the Osaka University as a Research Fellow. His research interests include developing the high-specific Raman imaging system and chemical screening technique by using Raman-tags.

Dr. Kawagoe is currently a Member of the Japan Society of Applied Physics (JSAP) and the Japan Society for Laser Microscopy.

Masahito Yamanaka received the B.S. and Ph.D. degrees in applied physics from Osaka University, Osaka, Japan, in 2006 and 2011, respectively.

After three years of experience as a Postdoctoral Fellow with the Japan Society for the Promotion of Science (JSPS) and the Funding Program for Next Generation World-Leading Researchers (NEXT program) in Osaka University, he joined the Department of Electronics in Nagoya University, Nagoya, Japan, as an Assistant Professor in 2014. His research interests include optical microscopy, optical coherence tomography/microscopy, and fiber lasers for biomedical imaging and analysis.

Dr. Yamanaka is currently a Member of the Japan Society of Applied Physics (JSAP), the Japan Society for Laser Microscopy, OSA, and SPIE.

Miyoko Matsushima received the B.S., M.S., and Ph. D. degrees in medical technology from Nagoya University, Nagoya, Japan, in 2002, 2004, and 2007, respectively. She was a Postdoctoral Fellow with Nagoya University, Nagoya, Japan, in 2007.

Since 2007, she has been working with Nagoya University School of Health Sciences as an Assistant Professor. In 2012, she became an Assistant Professor with the Pathophysiological Laboratory Sciences, Nagoya University Graduate School of Medicine, and in 2015, she becamea Lecturer.

Her scientific interests include development of devices for allergic test.

Kensaku Mori received the B.Eng. degree in electronics engineering, and the M.Eng. and Ph.D. degrees in information engineering from Nagoya University, Nagoya, Japan, in1992, 1994, and 1996, respectively. He is a Professor with the Graduate School of Informatics, Nagoya University, and the Director of Information Technology Center of Nagoya University and an MICCAI Fellow.

Dr. Mori is currently involved in many international conference organizations, including SPIE Medical Imaging, CARS, IPCAI and MICCAI, as a General Chair or program committee members. He is a Member of IEEE, SPIE, ISCAS, IEICE, JSCAS, JSMBE, and JAMIT. He was the recipient of many awards including Young Scientist Award from the Minister of Education, Culture, Sports, Science and Technology, and RSNA Magna Cum Laude.

Tsutomu Kawabe received the M.D. and Ph.D. degrees from Nagoya University, Nagoya, Japan, in 1987 and 1994, respectively. During graduated course, he was a special graduate research student at Osaka University, Japan.

In 1995, he was a Postdoctoral Fellow with the Memorial Sloan-Kettering Cancer Center, New York, NY, USA. In 1996, he was a Postdoctoral Associate with Rockefeller University, New York, NY, USA. In 1997, he worked as a Respirology Fellow with Nagoya University School of Medicine, Nagoya, Japan. Since 2004, he has been working with Nagoya University School of Health Sciences, Nagoya, Japan, as an Assistant Professor, as an Associate Professor in 2007, and as a Professor in 2009. In 2012, he became a Professor with the Pathophysiological Laboratory Sciences, Nagoya University Graduate School of Medicine. He was a Fellow with the Japanese Society of Internal Medicine, Tokyo, Japan.

His scientific interests include pathophysiology of respiratory diseases, development of devices for respiratory function test. Dr. Kawabe is a Board Certified Member of the Japanese Respiratory Society and the Japanese Society of allergy.